An optimal transformation method applied to diagnosing the ocean carbon sink

Neill Mackay[1], Jan D. Zika[2], Taimoor Sohail[2,3], Richard G. Williams[4], Oliver Andrews[5], and Andrew J. Watson[1]

[1]Faculty of Environment, Science and Economy, University of Exeter, UK
[2]School of Mathematics and Statistics, University of New South Wales, Sydney, Australia
[3]Centre for Excellence in Antarctic Science, University of New South Wales, Sydney, Australia
[4]School of Environmental Sciencies, University of Liverpool, UK
[5]Department of Environment and Geography, University of York, UK

Correspondence: Neill Mackay (n.mackay@exeter.ac.uk)

Abstract. The ocean carbon sink plays a critical role in climate, absorbing anthropogenic carbon from the atmosphere and mitigating climate change. The sink shows significant variability on decadal timescales, but estimates from models and observations disagree with one another, raising uncertainty over the magnitude of the sink, its variability, and its driving mechanisms. There is a need to reconcile observationally-based estimates of air-sea CO_2 fluxes with those of the changing ocean carbon inventory in order to improve our understanding of the sink, and doing so requires knowledge of how carbon is transported within the interior by the ocean circulation. Here we employ a recently developed Optimal Transformation Method (OTM) that uses water mass theory to relate interior changes in tracer distributions to transports and mixing and boundary forcings, and extend its application to include carbon using synthetic data. We validate the method using model outputs from a biogeochemical state estimate, and test its ability to recover boundary carbon fluxes and interior transports consistent with changes in heat, salt and carbon. Our results show that OTM effectively reconciles boundary carbon fluxes with interior carbon distributions when given a range of prior fluxes. OTM shows considerable skill in its reconstructions, reducing root-mean-squared errors from biased priors between model 'truth' and reconstructed boundary carbon fluxes by up to 71%, with bias of the reconstructions consistently $\leq 0.06\,\mathrm{mol\text{-}C\,m^{-2}\,yr^{-1}}$ globally. Inter-basin transports of carbon also compare well with the model truth, with residuals $< 0.25\,\mathrm{Pg\,C\,yr^{-1}}$ for reconstructions produced using a range of priors. OTM has significant potential for application to reconciling observational estimates of air-sea CO_2 fluxes with the interior accumulation of anthropogenic carbon.

1 Introduction

The ocean is an important sink for anthropogenic carbon ($\mathrm{C_{anth}}$), absorbing around 2.9 Pg C yr^{-1} in the most recent decade, which represents 27% of total emissions (Friedlingstein et al., 2022). The ocean carbon sink plays a role in mitigating atmospheric warming, but at a cost of the ocean acidifying which negatively impacts the ocean's ecosystem (Doney et al., 2009). Earth System models are sensitive to ocean carbon uptake (Arora et al., 2020), and understanding the mechanisms that govern its trends and variability is therefore crucial to accurate projection of both future climate change and its impacts. Estimates of

the ocean carbon sink from Global Ocean Biogeochemical Models (GOBMs) and surface ocean pCO_2-based data products show the carbon sink has been increasing in line with increases in atmospheric CO_2, but with significant variability (Hauck et al., 2020). The data products, which are based on gap-filling methods applied to surface ocean pCO_2 observations combined

25   with a gas transfer parameterization, have also suggested greater decadal variability and a steeper rate of increasing sink since the turn of the 21st century than GOBMs, and this inconsistency poses a challenge for attempts to characterise the sink (Rödenbeck et al., 2015). Furthermore, while estimates of the sink from GOBMs are fairly consistent globally, regionally differences are much larger (Fay and McKinley, 2021), pointing to deficiencies in the models' representations of underlying mechanisms.

    Variability in the ocean carbon sink has been linked to changes in the physical ocean circulation (DeVries et al., 2017;

30   Caínzos et al., 2022b). Ocean circulation can impact the sink both directly by physically transporting and mixing dissolved inorganic carbon (DIC) between the surface and deep ocean (Bopp et al., 2015), and indirectly by influencing changes in surface temperature, salinity and alkalinity that control surface pCO_2 (Halloran et al., 2015). The total sink thus results from a combination of C_{anth} uptake driven by rising atmospheric CO_2 concentrations, and variable fluxes of both C_{anth} and natural carbon (C_{nat}) driven by the redistribution of carbon and other tracers in the interior by the circulation.

35   A complete understanding of the ocean carbon sink cannot be attained without reconciling estimates of the air-sea flux with estimates of the changing inventory, including how carbon is redistributed in the interior. The rate of change of the global inventory of C_{anth} has been estimated at $2.6 \pm 0.3\,\mathrm{Pg\,C\,yr^{-1}}$ for the period 1994-2007 (Gruber et al., 2019), and this estimate has been shown as being consistent with the global air-sea flux, once corrections for a preindustrial riverine outgassing and a skin temperature effect on surface pCO_2 are taken into account (Watson et al., 2020). However, a comprehensive examination

40   of the consistency between estimates of the air-sea flux and the interior inventory changes at the level of ocean basins has so far only been possible through the use of data-assimilating ocean biogeochemical models, such as the ECCO-Darwin state estimate (Carroll et al., 2020, 2022). Such models are extremely useful in providing mechanistic understanding of the ocean carbon sink, however they are constrained by their resolution and parameterisation of subgrid-scale processes. Another approach using Green's functions (Haine and Hall, 2002) has been used to describe the transport of C_{anth} from the surface to

45   the interior (Khatiwala et al., 2009), but their methodology has the important caveat of assuming an ocean circulation in steady state.

    In this paper, we will present a novel method of estimating air-sea CO_2 fluxes that are consistent with changes in the ocean's carbon inventory and with interior transports and mixing of carbon. The method, termed the Optimal Transformation Method (OTM), uses a water mass coordinate system to determine the relative roles of ocean circulation, boundary fluxes and

50   interior mixing to changes in the ocean's interior tracer distributions. OTM was recently tested using outputs from a historical numerical climate model simulation, and was able to recover boundary fluxes of heat and freshwater closer to the 'true' model fluxes when biased fluxes were used as priors (Zika and Sohail, 2023). We will extend its application to carbon, and conduct a validation using model outputs from the ECCO-Darwin biogeochemical state estimate. OTM is an inverse method with a number of advantages over alternate approaches, enabled by its adoption of a water mass framework that simplifies the ocean

55   circulation with minimal loss of information. Firstly, the inverse approach can diagnose a physical tracer circulation consistent with observations with no requirement for the circulation to be in steady-state, and determine the transports and mixing of a

tracer such as carbon by that circulation. This feature is particularly useful for the carbon sink problem, in which the non-steady state circulation is known to play an important role in the variability (Gruber et al., 2023). Secondly, the water mass framework allows transports and mixing consistent with boundary forcing and interior changes to be diagnosed exactly, with no need to

60 impose a uniform vertical diffusion coefficient as has been done with previous inverse modelling involving carbon (Caínzos et al., 2022a). Finally, the method is computationally efficient when compared to data-assimilating numerical models, while retaining sufficient spatial resolution to facilitate analysis of mechanistic drivers of carbon sink variability. Once validated, OTM's extension to carbon can be applied to observations to produce a globally consistent estimate of ocean carbon uptake, transports and mixing.

65 The remaining sections of this paper are organised as follows: in section 2 an overview of the theoretical framework of OTM is provided including its extension to carbon. Section 3 presents the results of the validation of our method using model outputs from ECCO-Darwin, including comparisons of boundary carbon fluxes, and of transports of heat, freshwater and carbon, with the model 'truth'. Section 4 discusses the limitations of OTM and potential challenges for its future application to observations, and concludes.

70 ## 2   Methods

2.1   Water mass framework

Water mass methods work on the principle that the properties of a water mass, for example its heat, salt, or carbon content, can fundamentally only be altered by either tracer sources and sinks or interior mixing (Groeskamp et al., 2019). For a conservative tracer, sources and sinks are limited to boundary fluxes, usually at the sea surface. Walin (1982) first proposed a framework

75 relating temperature changes in the ocean interior to boundary heat fluxes and mixing; water mass theory has subsequently been built upon and applied many times to studying the ocean circulation (e.g. Speer, 1993; Nurser et al., 1999; Zika et al., 2012; Groeskamp et al., 2014; Hieronymus et al., 2014; Pemberton et al., 2015; Grist et al., 2016; Evans et al., 2017; Mackay et al., 2018; Zika et al., 2021; Sohail et al., 2021).

Recently, Zika and Sohail (2023) combined aspects of a Green's function approach with water mass theory to create the Optimal

80 Transformation Method. Here the method is briefly described; for full details the reader is referred to Zika and Sohail (2023). First, we define a set of 64 discrete water masses for the global ocean using the Binary Space Partitioning (BSP) method of Sohail et al. (2023), splitting the upper 2000 m of the ocean into equal volumes defined between upper and lower bounds in temperature (T) and salinity (S) on an unstructured grid. The upper and lower T and S bounds define the water masses used for our analysis. We then further split the ocean geographically into 9 basins, giving a total of 576 water masses globally, and

85 compute the volume of each water mass in each basin, this time for the full ocean depth, as well as their mass-weighted mean T and S (Fig. 1). The geographical region occupied by a water mass at a given point in time is defined by a three-dimensional mask $\Omega(\mathbf{x}, t)$. We also calculate the boundary fluxes, Q, of heat and freshwater into each water mass, integrated over the outcrop area of that water mass defined by $\Omega(x, y, 0, t)$, at each point in time (Eq. 9 and 10). All of these quantities are calculated as monthly means using model outputs from ECCO-Darwin (see section 2.3).
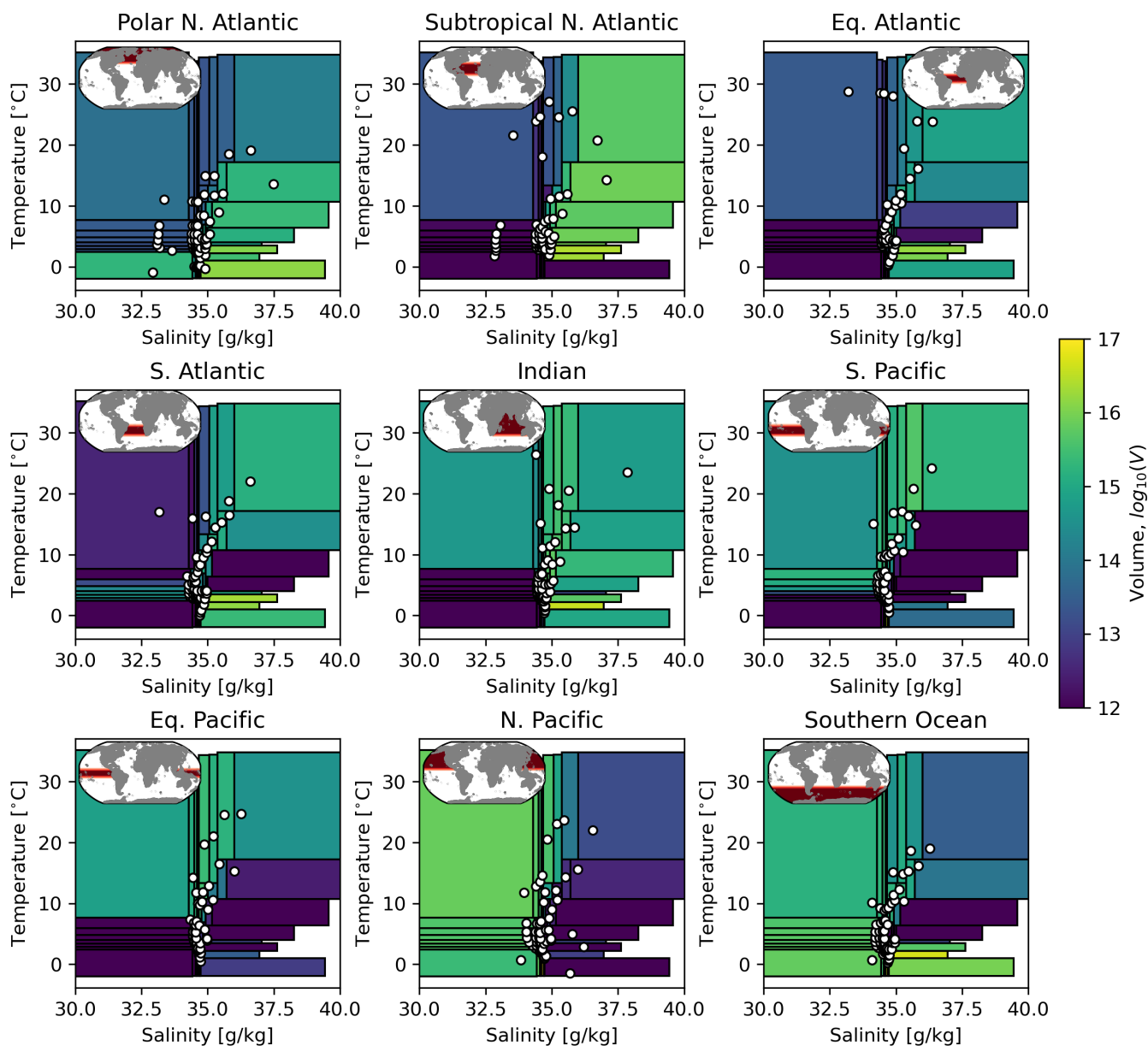
Figure 1. Water mass definitions from binary space partitioning (BSP) of ECCO-Darwin (early period time average 1995-2005). For each of nine ocean basins, the edges of the boxes show the global definitions of each water mass in temperature-salinity space, and the colours show the volume of water occupied by that water mass in that basin. The white dots show the volume-weighted mean temperature and salinity of each water mass for each basin. The inserts in the top left of each subplot show the geographical basin definitions.

We then seek to relate changes in the tracer distributions from an 'early' time period, with tracer concentrations $C_{0,i}$ in N water masses with mass $m_{0,i}$, to a 'late' time period, with tracer concentrations $C_{1,j}$ in N water masses of mass $m_{1,j}$, to boundary fluxes and interior transports and mixing. Effectively, the method minimises the misfit between an initial ($C_{0,i}$) and later ($C_{1,j}$) tracer distribution taking into account the boundary fluxes, Q_{ij}^{prior}, and the effect of a transport matrix $g_{i,j}$. We minimise a cost function which aims to find g_{ij} that is consistent with boundary fluxes and interior changes of tracer distributions:

$$[Cost function] = \sum_{j=1}^{N} \left\| w_j \left(\sum_{i=1}^{N} m_{0,i} g_{ij} \left(C_{0,i} + Q_{ij}^{prior} \right) - m_{1,j} C_{1,j} \right) \right\|^2. \tag{1}$$

The transport matrix represents the proportion of each early water mass i that becomes part of each late water mass j, and Q_{ij}^{prior} contains prior estimates of the boundary fluxes of each tracer that occur between the early and late time periods. When combined with the volumes and mean tracer concentrations computed in the BSP binning process (see above and Fig. 1), g_{ij} allows us to determine transports and mixing of tracers both between basins and between individual water masses within each basin. In Eq. 1, g_{ij} acts on the early tracer distribution that has been modified by the prior boundary fluxes. The weights, w_j, are chosen as:

$$w_j = \frac{1}{A_j} \left[\frac{1}{std(T)}, \frac{1}{std(S)} \right], \tag{2}$$

where A_j represents the water mass outcrop areas:

$$A_j = \frac{1}{t_1 - t_0} \int_{t_0}^{t_1} \int \int \Omega(x,y,0,t) dx dy dt, \tag{3}$$

and t_0 and t_1 are the midpoints of the early and late time periods. The standard deviations of T and S are the standard deviations of the time-dependent BSP-binned water mass mean T and S values. The weights effectively minimise the residual per unit outcrop area of each water mass, by more strongly penalising water masses with a small outcrop in the cost function, and normalise the contributions to the residual from different tracers. In order to avoid infinite weights where the outcrop area of a water mass is zero, the minimum value of a modified A_j is set to $min(A_j[A_j > 0])$, i.e. the smallest non-zero water mass outcrop area. The minimisation of the cost function is subject to the following constraints:

$$0 \le g_{ij} \le 1; \tag{4}$$

$$m_{1,j} = \sum_{i=1}^{N} m_{0,i} g_{ij}; \tag{5}$$

$$m_{0,i} = \sum_{j=1}^{N} m_{1,j} g_{ij}; \tag{6}$$

$$g_{ij} = 0 \text{ if } \Omega_i \text{ and } \Omega_j \text{ are not in the same or adjacent basins.} \tag{7}$$

Equation 4 above ensures that the transport matrix represents a fraction of the initial water mass volumes. Equations 5 and 6 impose conservation of mass for the sum of all the water masses. Equation 7 limits the geographical range of water mass
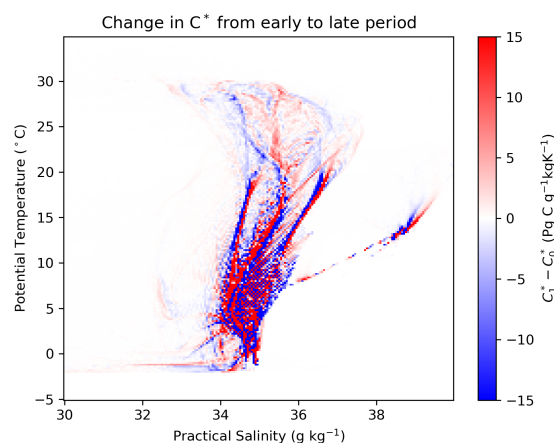
Figure 2. Changes in the amount of the conservative tracer C^* (see section 2.2) per unit temperature and salinity in ECCO-Darwin, from the early averaging period (1995-2005) to the late averaging period (2005-2015). Red indicates an increase in carbon in that region of T-S space; blue indicates a decrease.

interaction, excluding the possibility of unreaslistic tracer transport. We solve the optimisation problem for g_{ij} with the Python *cvxpy* package, using the 'MOSEK' solver with default settings.

2.2 Extension to carbon

120 In the above, we outlined our method in the context of its application to two conservative tracers: temperature and salinity. In order to extend its application to studying the ocean carbon sink, we use the tracer C^*, first proposed by Gruber et al. (1996), defined as:

$$C^* = DIC - R_{C:P}PO_4 - 0.5(ALK + R_{N:P}PO_4), \tag{8}$$

where DIC, PO_4 and ALK are Dissolved Inorganic Carbon concentration, Phosphate concentration and Alkalinity, respec-
125 tively, and $R_{C:P}$ and $R_{N:P}$ are C:P and N:P stochiometric ratios. C^* is quasi-conservative in the ocean, and in a model with fixed stochiometric ratios such as ECCO-Darwin, it should be exactly conservative. As such, within the context of this study C^* has the same property as T and S, that within a water mass it can only be modified by either boundary fluxes or mixing. We use the fixed ratios from ECCO-Darwin of $R_{C:P}$ = 120 and $R_{N:P}$ = 16. Fig. 2 shows changes in C^* in T-S space between an early period taken as the time-mean of the ECCO-Darwin tracer distributions from 1995-2005, and a late period taken as the
130 time-mean of the tracer distributions from 2005-2015. The differences in the distributions of T, S, and C^* between these two periods, and the boundary fluxes of those three tracers, form the basis for the application of OTM in this study. In setting up our inverse problem (Eq. 1), we use the same water masses, defined in T-S coordinates, as plotted on Fig. 1, with the mass-weighted mean C^* in each water mass incorporated as additional elements of C.

We test two distinct implementations of the incorporation of carbon into OTM. In the first implementation, there is no prior

estimate of the boundary carbon flux and the optimisation to minimise the cost function in Eq. 1 is carried out inputting (i) the concentrations of T and S for the two time periods, and (ii) the boundary fluxes Q_{ij}^{prior} for heat and freshwater, which are calculated from the ECCO-Darwin surface forcing as follows:

$$Q_{i,T}^{prior} = \frac{1}{\rho_0 C_p m_{0,i}(t_1 - t_0)} \int_{t_0}^{t_1} \int \int \Omega_i(x,y,0,t)\, q_T(x,y,t)\, dx dy dt \qquad (9)$$

$$Q_{i,S}^{prior} = \frac{1}{\rho_0 m_{0,i}(t_1 - t_0)} \int_{t_0}^{t_1} \int \int \Omega_i(x,y,0,t)\, (q_S(x,y,t) - S_0\, q_{FW}(x,y,t) + q_{SP})\, dx dy dt. \qquad (10)$$

Here ρ_0 is a reference density = $1029\ \mathrm{kg\,m^{-3}}$, C_p is the heat capacity of seawater = $4000\ \mathrm{J\,kg^{-1}\,K^{-1}}$, q_T is the surface heat flux in $\mathrm{W\,m^{-2}}$, q_S is the surface salt flux in $\mathrm{g\,m^{-2}\,s^{-1}}$, S_0 is a reference salinity = $35\ \mathrm{g\,kg^{-1}}$, q_{FW} is the surface freshwater flux in $\mathrm{kg\,m^{-2}\,s^{-1}}$, and q_{SP} is the depth-summed salt tendency due to salt plume flux from sea ice formation in $\mathrm{g\,m^{-2}\,s^{-1}}$. In this case, the transport solution g_{ij} represents transports that are consistent with the changing T and S distributions and the surface heat and salt/freshwater boundary fluxes. We impose constraints on transport matrix g_{ij} for the volume transport through Bering Strait, which is set to 1.1 Sv northwards ($1\ \mathrm{Sv} = 10^6\ \mathrm{m^3\,s^{-1}}$), and the Indonesian throughflow, which is set to a net transport of 15 Sv westwards, based on volume transports from ECCO-Darwin. Having obtained the transport matrix g_{ij}, we then estimate the boundary carbon flux from the residual between the final C* distribution, $C_{1,j}$, and the initial C* distribution, $C_{0,i}$, modified by the transport g_{ij}:

$$Q_j^{adjust} = C_{1,j} - \frac{1}{m_{1,j}} \sum_{i=1}^{N} m_{0,i} g_{ij} C_{0,i}. \qquad (11)$$

Note that for obtaining the C* adjustment we use the BSP-binned mean carbon concentrations for C in Eq. 11; we can equally obtain the adjustments in T and S , but these mismatches are small since we have used the exact boundary forcings for heat and freshwater as priors.

In the second implementation, we include a prior estimate of the boundary carbon flux, which we modify with estimates of the uncertainty (see section 2.3), and include all three tracers (T, S and C*) in the minimisation of Eq. 1. In this case, the weights are:

$$w_j = \frac{1}{A_j} \left[\frac{1}{std(T)}, \frac{1}{std(S)}, \frac{1}{std(C^*)} \right], \qquad (12)$$

and the unmodified carbon flux is:

$$Q_{i,C^*}^{prior} = \frac{1}{m_{0,i}(t_1 - t_0)} \int_{t_0}^{t_1} \int \int \Omega_i(x,y,0,t)\, q_{CO2}(x,y,t) - \Omega_i(x,y,D,t)\, q_{sed}(x,y,t)\, dx dy dt, \qquad (13)$$

where q_{CO2} is the air-sea CO_2 flux, D is the water depth at (x,y), and q_{sed} is the sediment flux of C* due to falling particulate matter, which in ECCO-Darwin is removed from the model when particulate matter hits the sea floor. The mask Ω_i is applied such that q_{CO2} acts at the surface and q_{sed} acts at the sea floor. The sediment flux is calculated as:

$$q_{sed} = \mathrm{POC}\, w_{\mathrm{POC}} - \mathrm{R_{C:P}}\, \mathrm{POP}\, w_{\mathrm{POP}} - \frac{\mathrm{R_{N:P}}}{2}\, \mathrm{POP}\, w_{\mathrm{POP}}, \qquad (14)$$

where POC and POP are the particulate organic carbon and particulate organic phosphorus concentrations, respectively, in the bottom wet grid cell of the model, $w_{\text{POC}} = w_{\text{POP}} = 10$ m/day are the sinking rates for particulate organic carbon and particulate

165 organic phosphorus, and $R_{\text{C:P}}$ and $R_{\text{N:P}}$ are stochiometric ratios as in Eq 8. For this implementation, OTM seeks a transport matrix g_{ij} that is consistent with the prior fluxes and interior changes of T, S, and C^*, minimising the adjustment for all three tracers as diagnosed from Eq. 11.

2.3 Validation with numerical model output

The ECCO-Darwin model (Carroll et al., 2020) is an ocean biogeochemical model based on the ECCO state estimate (Forget

170 et al., 2015), coupled online to the MIT Darwin ecosystem model (Dutkiewicz et al., 2015). ECCO uses an adjoint of the MITgcm to assimilate all available physical observations into an internally-consistent tracer-conserving estimate of the physical ocean state that matches well the observational data while obeying the model's dynamical equations. Meanwhile the Darwin component is optimised using a Green's function approach to obtain the best fit to biogeochemical observations. ECCO-Darwin is run from 1992-2017, and we use monthly mean outputs from January 1995 - December 2015 for validating our

175 Optimal Transformation Method. The model has 50 vertical levels and uses the ECCO LLC270 horizontal grid, which has 13 tiles of 270 x 270 grid cells each, and a horizontal grid spacing of between $1/3°$ at the equator and $\sim$18 km at high latitudes (Carroll et al., 2020).

An important feature of ECCO-Darwin that makes it a good choice for this study is that the budgets of heat, freshwater and C^* are closed over the time period covered by the model outputs we are using. Confirming that these budgets close globally

180 is a good check that the principle underpinning OTM, that only boundary fluxes or interior mixing can change water mass properties for conservative tracers, will hold. The heat, freshwater and carbon budgets computed from the BSP-binned values that we input to OTM are shown on Fig. A1. There are small offsets in the heat and freshwater budgets because we have used monthly mean fields, which introduces a temporal error. In the carbon budget there is a budget residual of around 3% that accumulates over the second half of the time period. This residual is most likely due to slight differences between our

185 calculation of the sediment flux of C^*, which itself is not a model variable but which we calculate from equation 8, and the loss of C^* to the model's bottom boundary. In any case, the residual is smaller than we might hope to achieve when applying our method to observations in a future study. This residual places a lower limit on the residual that we can expect from our OTM optimisations.

In order to assess the ability of OTM to obtain a consistent estimate of the uptake, transports and mixing of carbon from

190 imperfect information, we test 5 cases with different priors for the boundary carbon flux. The first case uses no prior, as already outlined in section 2.2. Case 2 uses the ECCO-Darwin model fluxes binned into water mass space (Eq. 13), which is as close to the model 'truth' as can be achieved with this method (see Fig. 5). For cases 3-5, we construct a 2D field of uncertainties on the air-sea CO_2 flux based on an ensemble of observational estimates compiled by Fay et al. (2021), which combines 6 different observationally-based pCO_2 data products with 5 different wind products via a gas transfer parameterisation to

195 produce 30 different air-sea CO_2 flux estimates. We calculate an observational uncertainty as the standard deviation of the time-mean of these 30 estimates at every gridpoint, and use that as the basis for uncertainties on our CO_2 flux priors. The

gridded uncertainties are shown on Fig. A2. For cases 3 and 4, we add a negative and a positive bias with a magnitude of 2x the observational uncertainties (i.e. 2-sigma or 95% confidence interval) to the ECCO-Darwin air-sea CO_2 flux at each gridpoint, before computing the BSP-binned Q_{i,C^*}^{prior} using equation 13, giving us lower and upper bounds (Fig. 4g and 4j). For case 5,

200   a bias of 2x the observational uncertainty but of the same sign as the ECCO-Darwin flux is applied, meaning that fluxes are biased in the direction of the prior flux (either into or out of the ocean; Fig. 4m).

2.4 Remapping into geographical coordinates

The information contained in the priors and raw OTM solutions is organised according to the 576 water masses defined in the BSP binning process. To aid interpretation, we map the solutions for the carbon fluxes and their priors back into geographical

205   coordinates using a time average over the 1995-2005 'early' period of the mask used for the BSP binning, such that $q(x,y,z)$ is the carbon flux in cartesian coordinates:

$$q(x,y,z)^{prior} = \sum_{i=1}^{N} \frac{1}{(t_1 - t_0)} Q_i^{prior} \Omega_i(x,y,z) \tag{15}$$

$$q(x,y,z)^{mix} = \sum_{j=1}^{N} \frac{1}{(t_1 - t_0)} Q_j^{mix} \Omega_i(x,y,z) \tag{16}$$

$$q(x,y,z)^{adjust} = \sum_{j=1}^{N} \frac{1}{(t_1 - t_0)} Q_j^{adjust} \Omega_i(x,y,z), \tag{17}$$

210   where:

$$Q_j^{mix} = \frac{1}{m_{1,j}} \left[\sum_{i=1}^{N} m_{0,i} g_{ij} \left(C_{0,i} + Q_i^{prior} \right) \right] - C_{0,i=j} - Q_{i=j}^{prior} \tag{18}$$

is the effect of transports and mixing on each tracer. The depth-integrated carbon flux at each grid point is calculated as:

$$q(x,y) = \sum_z \left[q^{prior}(x,y,z) + q^{adjust}(x,y,z) \right], \tag{19}$$

i.e. the sum over all depth of the prior plus the adjustment for the carbon fluxes. Note that Eq. 19 calculates the depth-integral

215   of the carbon flux remapped from water mass space using three-dimensional masks (Eq. 15 and 17), and which results from a combination of the air-sea flux and the sediment flux. This depth-integrated carbon flux is not the same as the air-sea flux acting on the surface water mass outcrops; the three-dimensional remapping is to ensure that our remapped fields include all sources and sinks of C^*, since not all water masses with an associated sediment flux have a surface outcrop. Our aim is to assess the ability of OTM to reconstruct the ECCO-Darwin boundary fluxes for a closed carbon budget.
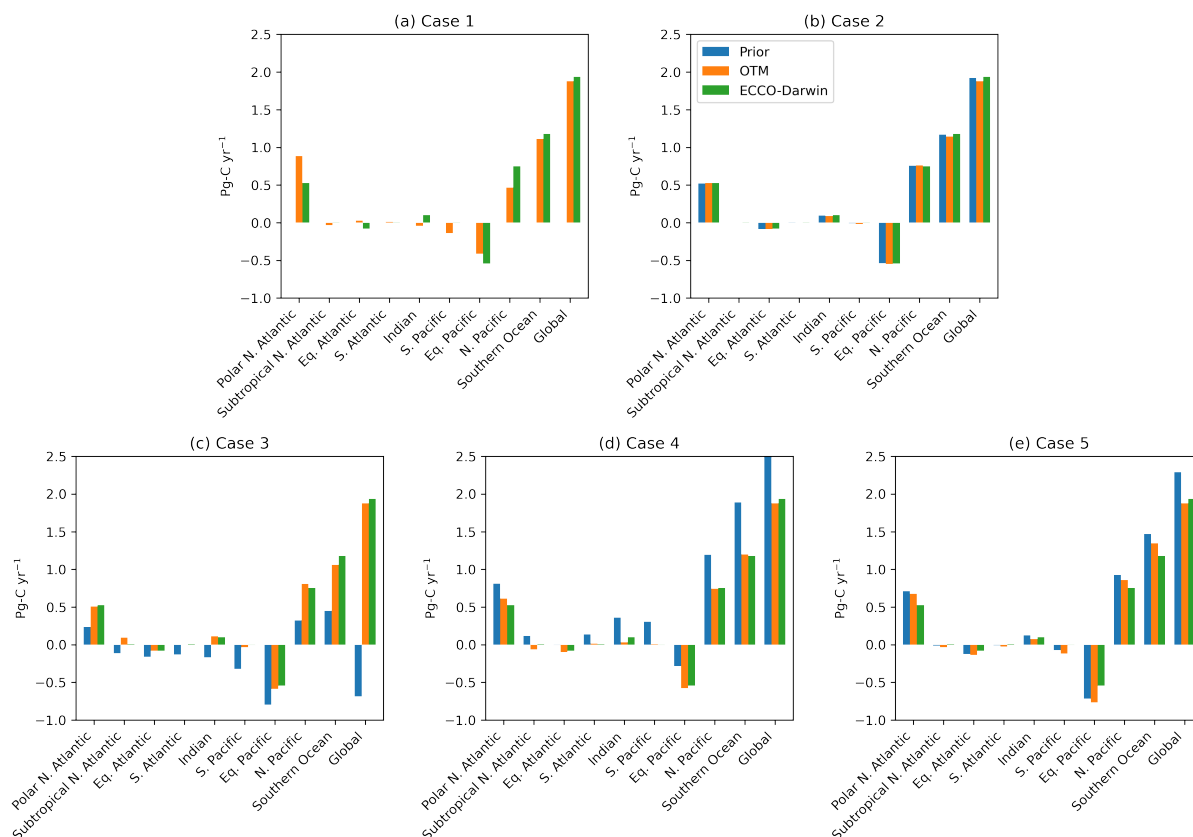
Figure 3. Basin-integrated carbon fluxes (positive into the ocean) from five cases with different priors. Blue bars show the prior fluxes, orange bars show the OTM solutions, and green bars show the ECCO-Darwin model 'truth'. Note that on panel (d) the prior global flux is $4.5 \, \mathrm{Pg \, C \, yr^{-1}}$; the y-axis is cut off for ease of comparison with the other cases.

3 Results

3.1 Carbon sink

For case 1, where OTM is given no prior carbon flux and the cost function is minimised by only considering the changes in T and S distributions and their associated boundary fluxes, when integrated over each basin the agreement between the OTM solution and the ECCO-Darwin model truth is generally good (Fig. 3a). The exceptions are in the Polar North Atlantic, where OTM has overestimated the uptake, and in the North Pacific, where it is underestimated. When remapped into geographical coordinates, it is more obvious where OTM has struggled to converge towards the model truth with limited information (Fig. 4a and 4b). The RMSE between the model truth and the prior/solution reduces from $0.89 \, \mathrm{mol\text{-}C \, m^{-2} \, yr^{-1}}$ to $0.76 \, \mathrm{mol\text{-}C \, m^{-2} \, yr^{-1}}$, and the bias reduces from $-0.36 \, \mathrm{mol\text{-}C \, m^{-2} \, yr^{-1}}$ to $0.07 \, \mathrm{mol\text{-}C \, m^{-2} \, yr^{-1}}$.

For case 2, where OTM is given an ideal prior carbon flux based on the model truth and the cost function is minimised for T, S
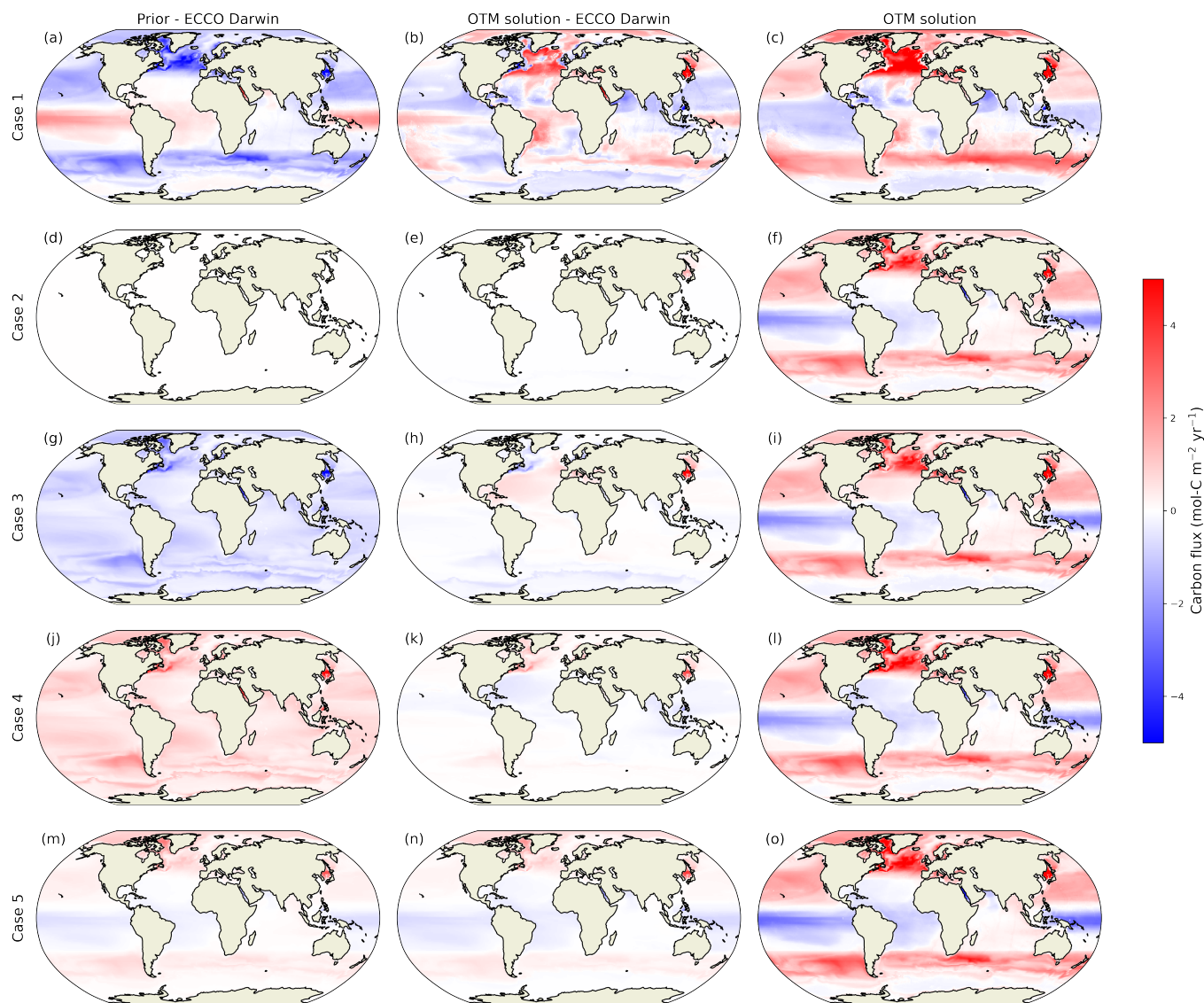
Figure 4. OTM solutions from five cases with different carbon flux priors, remapped into geographical space. Left column shows the carbon flux difference between the prior and the ECCO-Darwin model 'truth'; middle column shows the difference between the OTM solution and the model truth; and right column shows the OTM solution. Top row shows the solution for case 1 with no carbon flux prior; second row shows case 2 where a prior based on the model truth was used; rows 3 and 4 show cases 3 and 4 where the prior fluxes included a bias of two times an a-priori uncertainty calculated at each grid point; and bottom row shows case 5 where double the a-priori uncertainty was applied as a bias with the same sign as the prior flux (see section 2.3). Red and blue indicate either positive and negative biases compared to the model truth (panels a, b, d, e, g, h, j, k, m, n) or fluxes into and out of the ocean (panels c, f, i, l, o).

and C^*, the basin-integrated solution is close to the model truth for all basins (Fig. 3b). For the remapped fluxes (Fig. 4d, and 4e) there is a small region in the sea of Japan where OTM has drifted slightly away from the model truth, but across the rest of the ocean the solution matches the model very closely. The RMSE between the model truth and the prior/solution increases slightly from 0.00 to 0.04 $\mathrm{mol\text{-}C\,m^{-2}\,yr^{-1}}$, and the bias increases fractionally from 0.00 to -0.01 $\mathrm{mol\text{-}C\,m^{-2}\,yr^{-1}}$.

For cases 3 and 4, where the prior carbon fluxes represent 95th percentile lower and upper bounds, respectively, based on an observational uncertainty estimate, the adjustment away from the priors towards the model truth in the basin-integrated OTM solutions is striking (Fig. 3c and 3d). Examining the remapped fluxes for case 3, the bias is reduced across most of the ocean, with small negative biases remaining in the Southern Ocean and Western Subpolar North Atlantic, and positive biases in the Subtropical North Atlantic and the Sea of Japan (Fig. 4h). The RMSE reduces almost two thirds from 0.59 to 0.22 $\mathrm{mol\text{-}C\,m^{-2}\,yr^{-1}}$, and the bias nearly disappears, going from -0.41 to -0.02 $\mathrm{mol\text{-}C\,m^{-2}\,yr^{-1}}$. Case 4 shows the greatest improvement from prior to solution, with the RMSE reducing from 0.59 to 0.18 $\mathrm{mol\text{-}C\,m^{-2}\,yr^{-1}}$ and the bias from 0.41 to 0.02 $\mathrm{mol\text{-}C\,m^{-2}\,yr^{-1}}$. Similar to case 3, there are patches of bias in the solution in the North Atlantic and the Sea of Japan.

Case 5 tests the limits of the method's capability: basin-integrated fluxes are close to the model truth, and tend to be moving away from the prior and towards the truth in the basins with larger fluxes and especially globally (Fig. 3e). However, in the Equatorial Pacific the basin-integrated solution is further from the truth than the prior, and the remapped fluxes do not show an obvious improvement from prior to solution (Fig. 4m and 4n). The RMSE reduces slightly from 0.33 to 0.29 $\mathrm{mol\text{-}C\,m^{-2}\,yr^{-1}}$, and the bias reduces from 0.12 to 0.05 $\mathrm{mol\text{-}C\,m^{-2}\,yr^{-1}}$.

The remapped OTM solutions from cases 2-5 are very similar to each other across most of the ocean (Fig. 4f, 4i, 4l, and 4o), and with the remapped model truth, shown on Fig. 5b. The latter gives a visual representation of the best theoretical solution that can be obtained with this method, when binning each of 9 basins into 64 water masses using the BSP binning process and then remapping back into geographical coordinates. The original model fluxes are shown on Fig. 5a for comparison. The case 1 solution (Fig. 4c) is broadly similar to the model truth in terms of the main regions of uptake and outgassing, indicating that T and S constraints alone provide a good first guess on the redistribution of carbon as a means of estimating the boundary carbon fluxes when combined with the interior changes in C^*. This is then improved by the addition of the prior boundary carbon flux Q_{i,C^*}, and the inclusion of carbon in the cost function (Eq 1), in cases 2-5.

3.2 Meridional tracer transports

We can also validate our OTM solutions with respect to meridional transports of heat, freshwater, and carbon, at the boundaries between our 9 ocean basins. These are obtained for the OTM solutions by combining the transport matrix g_{ij} with the time-mean over the early period of the water-mass mean tracer values calculated during the BSP binning process, T_0, S_0, and C_0^*, modified by their prior boundary fluxes, as follows:

$$[Heat\ transport]^{OTM} = C_p \rho_0 \sum_{i=1}^{N} m_{0,i}(T_{0,i} + Q_{i,T}^{prior})g_{ij}\delta_{ij} \tag{20}$$
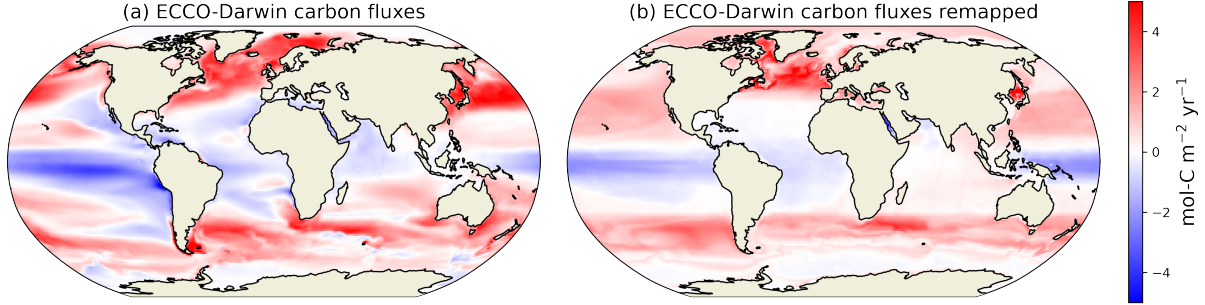
Figure 5. Boundary carbon fluxes (air-sea CO_2 flux - sediment flux) for the ECCO-Darwin 1995-2015 time-mean (a) and the BSP-binned fluxes remapped back into geographical coordinates (b).

$$[Freshwater\ transport]^{OTM} = \frac{-\rho_0}{S_0} \sum_{i=1}^{N} m_{0,i}(S_{0,i} + Q_{i,S}^{prior}) g_{ij} \delta_{ij} \tag{21}$$

$$[Carbon\ transport]^{OTM} = \sum_{i=1}^{N} m_{0,i}(C_{0,i}^{*} + Q_{i,C^*}^{prior}) g_{ij} \delta_{i,j}, \tag{22}$$

where $\delta_{ij} = 1$ if water mass i is upstream of the boundary between two basins, and j is downstream, $\delta_{ij} = -1$ if j is upstream and i is downstream, and $\delta_{ij} = 0$ for unconnected basins. We obtain the comparable meridional transports from ECCO-Darwin from the residual between the latitude-integrated air-sea fluxes and interior changes:

$$[Heat\ transport]^{E-D}(y') = \frac{1}{t_1 - t_0} \int_{t_0}^{t_1} \int_{y=0}^{y'} \int q_T(x,y,t)\ dxdydt$$

$$-\frac{C_p \rho_0}{t_1 - t_0} \int \int_{y=0}^{y'} \int [T(x,y,z,t_1) - T(x,y,z,t_0)]\ dxdydz \tag{23}$$

$$[Freshwater\ transport]^{E-D}(y') = \frac{-\rho_0}{S_0(t_1 - t_0)} \int_{t_0}^{t_1} \int_{y=0}^{y'} \int \left[q_S(x,y,t) - \frac{S_0}{\rho_0} q_{FW}(x,y,t) + q_{SP} \right] dxdydt$$

$$+\frac{\rho_0}{S_0(t_1 - t_0)} \int \int_{y=0}^{y'} \int [S(x,y,z,t_1) - S(x,y,z,t_0)]\ dxdydz \tag{24}$$
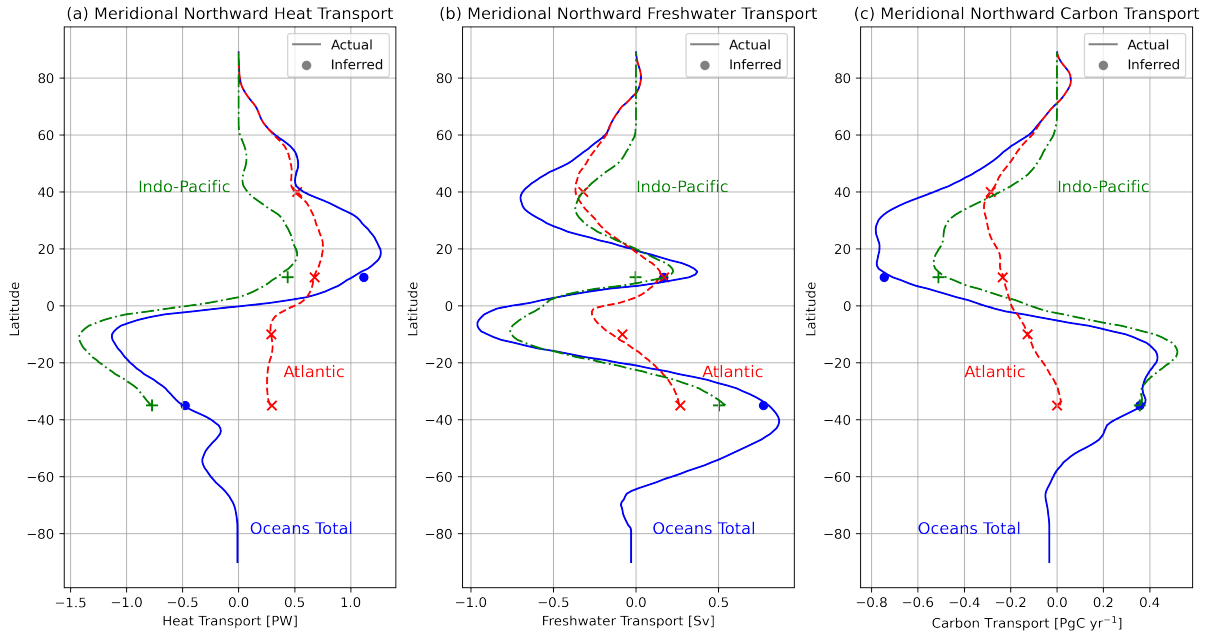
Figure 6. Zonally-integrated meridional transports of (a) heat, (b) freshwater, and (c) carbon from ECCO-Darwin at all latitudes (lines) and their equivalents from the case 2 OTM solution at the latitudes of the inter-basin boundaries (point markers). In blue (solid lines/dots) are the globally integrated transports, in green (dot-dashed lines/pluses) are the transports integrated over the Indian and Pacific oceans, and in red (dashed lines/crosses) the transports integrated over the Atlantic ocean.

$$[Carbon\ transport]^{E\text{-}D}(y') = \frac{1}{t_1 - t_0} \int\limits_{t_0}^{t_1} \int\limits_{y=0}^{y'} \int [q_{CO2}(x,y,t) - q_{sed}(x,y,t)]\ dxdydt$$

$$- \frac{1}{t_1 - t_0} \int \int\limits_{y=0}^{y'} \int [C^*(x,y,z,t_1) - C^*(x,y,z,t_0)]\ dxdydz. \tag{25}$$

The integrations in equations 23-25 are done globally, and then separately for the Atlantic and Indo-Pacific using a mask. For the Atlantic and Indo-Pacific comparisons, the OTM values calculated from equations 20-22 have subtracted from them

275   a northward transport of heat, freshwater or carbon that flows through Bering Strait. This correction is necessary because the Atlantic mask includes the Arctic Ocean, and the Indo-Pacific mask excludes it, which means the integrations implicitly assume that all of the residual between the boundary fluxes and interior changes results in meridional transports flowing through the Atlantic, when in reality the transports are split between the two.

The comparison between the meridional transports of heat, freshwater and carbon obtained from the OTM case 2 solution

280   and ECCO-Darwin is shown on Fig. 6. For this experiment, the OTM transports are very close to the model truth for all three tracers at almost all latitudes where we can make comparisons at inter-basin boundaries, both globally, and separately for the
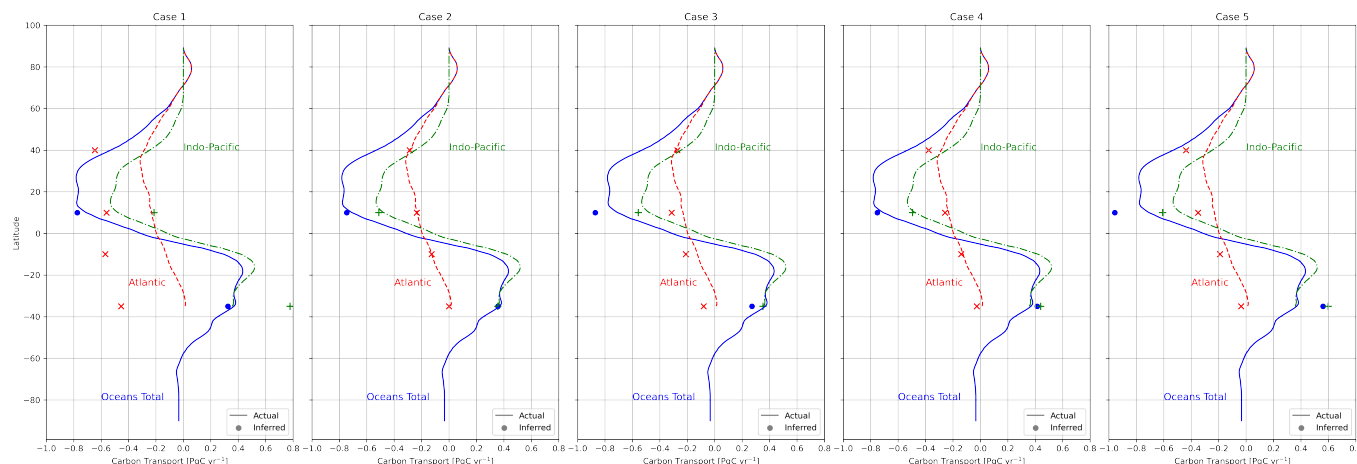
Figure 7. Zonally-integrated meridional transports of carbon from ECCO-Darwin at all latitudes (lines) and their equivalents from OTM solutions for cases 1-5 at the latitudes of the inter-basin boundaries (point markers). In blue (solid lines/dots) are the globally integrated transports, in green (dot-dashed lines/pluses) are the transports integrated over the Indian and Pacific oceans, and in red (dashed lines/crosses) the transports integrated over the Atlantic ocean.

Atlantic and Indo-Pacific. There is a residual of ∼0.2 Sv of freshwater transport at 10°N in the Indo-Pacific, which can be regarded as a much smaller residual in the latitude at which the transport zero-crossing occurs, since the green line crosses over the position of the green dot just to the south of it. The heat and freshwater transports from the OTM solutions for cases 1, 3, 4, and 5 are nearly identical to those of case 2 in Fig. 6 and are not plotted; however, there is some variation in the solutions for carbon (Fig. 7). The discrepancies between OTM and ECCO-Darwin are fairly small for cases 3 and 4, but for case 1, although the transports match well globally at 10°N and 35°S, the southward transport in the Atlantic is significantly overestimated, and meanwhile the Indo-Pacific transports are offset northwards by a similar amount. This mismatch indicates that OTM is unable to recover the correct transports of carbon solely from information about the changes in temperature and salinity and associated boundary fluxes of heat and salt/freshwater. Nonetheless, the reasonable agreement between the basin-integrated OTM carbon fluxes and the model truth for case 1 on Fig. 3a is encouraging, suggesting that even with limited information OTM gets the divergences in carbon transports approximately correct. For case 5, slightly too much southward transport in the Northern Hemisphere in both the Atlantic and Indo-Pacific combines such that the global mismatch at 10°N is worst for this experiment. At 35°S, the Indo-Pacific and global northward transports are similarly overestimated by OTM. Overall, the spread in the estimates of meridional tracer transports across cases 2-5 is < 0.30 Pg C yr^{-1}, and the mismatch between the OTM solutions and the model truth is < 0.25 Pg C yr^{-1}.

3.3 Basin carbon budgets

The net inter-basin carbon transports from the case 2 OTM solution are shown on Fig. 8, along with the boundary carbon fluxes (air-sea flux - sediment flux). The overall picture is of a convergence of meridional carbon transports and accompanying surface
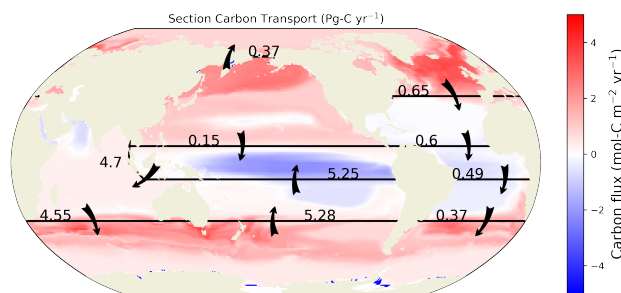
Figure 8. Inter-basin net transports of carbon (black arrows) and the boundary carbon flux (background colours, positive into the ocean) for the case 2 OTM solution. Transports are in Pg C yr^{-1}
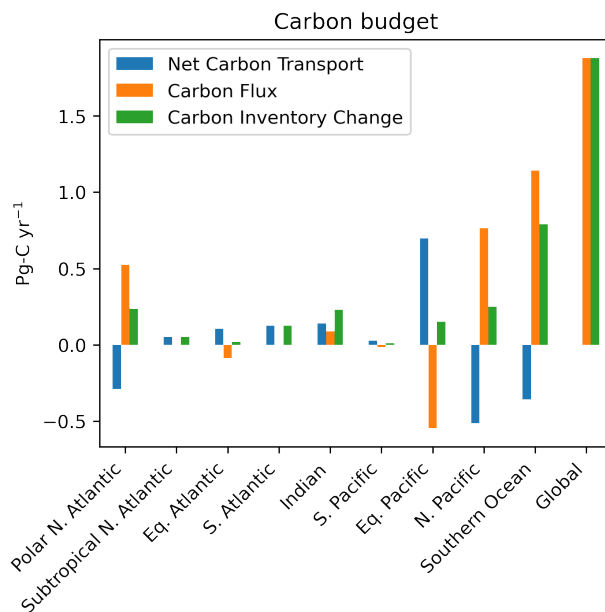
Figure 9. Carbon budget in each basin for the case 2 OTM solution. Blue bars show the net carbon transports, orange bars show the carbon flux (positive into the ocean), and green bars show the inventory change.

300 outgassing between 10°N and 10°S, and a divergence of transports and accompanying surface uptake at higher latitudes. A large counter-clockwise circulation of carbon between the Southern Ocean, the South Pacific and the Indian Ocean may be an instance where the OTM solution departs from reality that is not evident from the zonally integrated comparisons on Fig. 6; possible reasons for this will be discussed in section 4.1. Integrating the transport divergences, boundary fluxes, and interior changes allows us to construct a carbon budget for each basin (Fig. 9 and Table A1). The largest changes occur

305 in the Polar North Atlantic, Equatorial Pacific, North Pacific, and Southern Ocean. In the Polar North Atlantic, an uptake of $0.52 \, \text{Pg C yr}^{-1}$ is balanced by a roughly even split between a net transport of $-0.29 \, \text{Pg C yr}^{-1}$ out of the basin and an increase
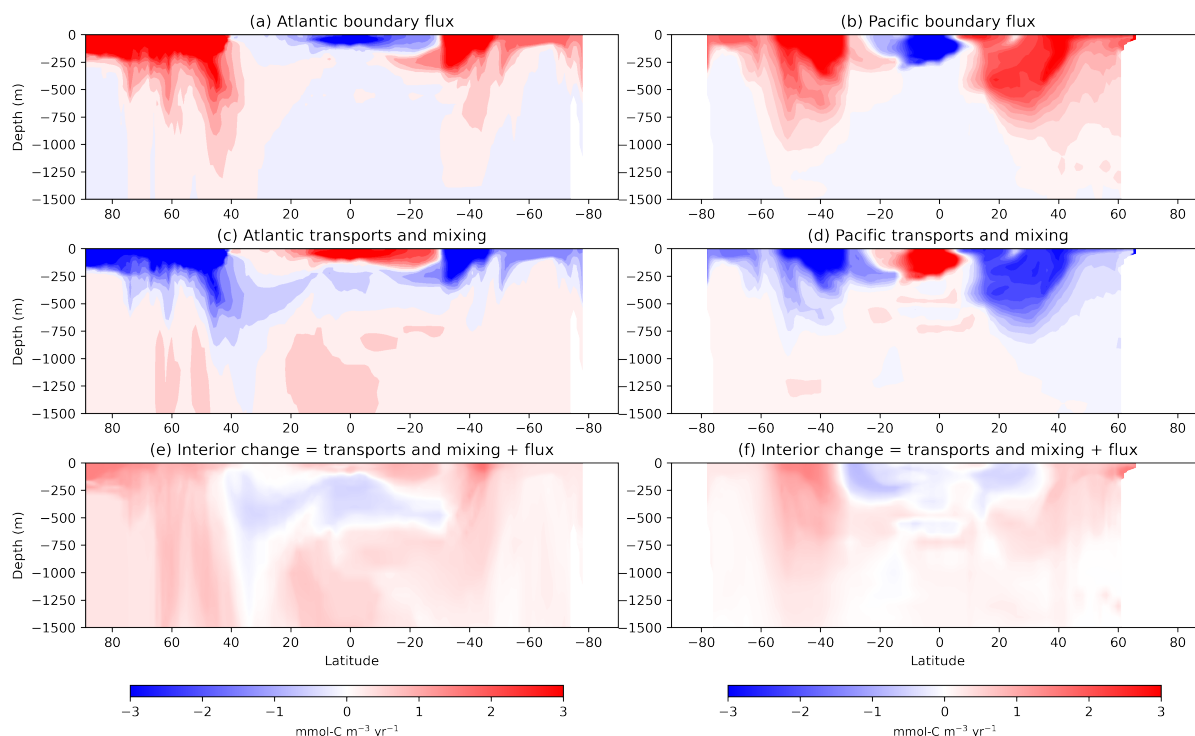
Figure 10. Zonally-averaged interior carbon concentration changes from the case 2 OTM solution in the Atlantic (left column) and the Pacific (right column) for the top 1500 m of the ocean. Top row shows the impact of carbon fluxes (air-sea flux + sediment flux) in or out of the ocean on the carbon concentrations; middle row shows the impact of transports and mixing; and bottom row shows the interior changes, which is the sum of the first two rows. Positive values are increases in carbon concentrations between our early (1995-2005) and late (2005-2015) averaging periods due to each component, and negative values are decreases over that time.

in the basin's inventory of $0.24\,\mathrm{Pg\,C\,yr^{-1}}$. In the Equatorial Pacific, a transport of $0.70\,\mathrm{Pg\,C\,yr^{-1}}$ into the basin is balanced by an outgassing of $-0.55\,\mathrm{Pg\,C\,yr^{-1}}$ and a small increase in the basin's inventory of $0.15\,\mathrm{Pg\,C\,yr^{-1}}$. In the North Pacific, roughly the reverse happens, with an uptake of $0.76\,\mathrm{Pg\,C\,yr^{-1}}$ balanced by a transport out of the basin of $-0.51\,\mathrm{Pg\,C\,yr^{-1}}$ and an inventory increase of $0.25\,\mathrm{Pg\,C\,yr^{-1}}$. Finally in the Southern Ocean, an uptake of $1.14\,\mathrm{Pg\,C\,yr^{-1}}$ goes mainly into an inventory increase of $0.79\,\mathrm{Pg\,C\,yr^{-1}}$, with a smaller transport of $-0.36\,\mathrm{Pg\,C\,yr^{-1}}$ out of the basin. Globally, the budget is closed, with an uptake of $1.88\,\mathrm{Pg\,C\,yr^{-1}}$ balanced by an equal increase in inventory.

3.4 Interior remapping of OTM solutions

So far, we have examined the OTM solutions in terms of a depth-integrated view of exchanges between basins and boundary forcings. We can also analyse the three-dimensional remapped fields from Eqs. 15 - 17 to explore the contributions of boundary fluxes versus transports and mixing to changes in the ocean interior. Zonal mean sections of these components, and their sum

which by construction equals the inventory change, for the Atlantic and Pacific are shown for the top 1500 m on Fig. 10, and for the full ocean depth on Fig. A3. Note that remapping the components using the 3D mask $\Omega_i(x, y, z)$ means the carbon changes are averaged over the full geographical extent of each water mass in the ocean interior, which implies the assumption

320 that each water mass is homogenous, i.e. that they have been well-mixed over the 10-year timescale under consideration. In the Atlantic, boundary fluxes cause an invasion of carbon in the northern high latitudes into water masses that penetrate to greater depths moving equatorwards, with a maximum around 40°N (Fig. 10a). A similar pattern appears in the south Atlantic, with an additional penetration to ~ 500 m depth near Antarctica. Meanwhile, outgassing water masses in the lower lattitudes are confined to the the top ~ 200 m. In the Pacific, patterns are similar also, but there is greater penetration to depth in the

325 southern hemisphere, and the outgassing layer reaches deeper but over a narrower range of latitudes (Fig. 10b). Transports and mixing move carbon away from high latitudes where the atmosphere provides a carbon source, and towards low latitudes in the shallower waters in both the Atlantic and the Pacific, to where the atmosphere provides a carbon sink; hence the transport and mixing opposes the effect of the surface flux (Fig. 10c and 10d). In the Atlantic low latitudes transports and mixing move carbon away from the region just below the surface, dominating the interior change and causing a net loss of carbon between

330 ~ 40°N and ~ 30°S and ~ 150 - 700 m depth (Fig. 10c and 10e). In the Pacific, transport dominates in the subtropical cells, causing a net loss of carbon between ~ 30°S and ~ 40°N and up to ~ 500 m depth; this signal may be due to wind-driven subduction of carbon from the mixed layer. In the Atlantic, transports and mixing between ~ 750 - 2000 m depth cause net accumulation in the equatorial and northern subpolar regions (Figs. A3c and A3e). In the deeper waters, transports and mixing lead to a reduction in carbon concentrations between ~ 40°N and ~ 30°S below ~ 3000 m (Fig. A3c and A3e); this signal

335 is likely an imprint of the Atlantic Meridional Overturning Circulation, upwelling in the Southern Ocean before returning northwards and supplying carbon from the deep ocean to be later outgassed at lower latitudes.

4 Discussion

4.1 Limitations of the Optimal Transformation Method

The Optimal Transformation Method may be used to diagnose interior transports and mixing of carbon consistent with bound-

340 ary fluxes and interior changes, and for recovering the true boundary fluxes from biased priors, when applied to model data where perfect information is available. When given information limited to changes in temperature and salinity distributions and their boundary forcings, OTM obtains a transport matrix that is broadly consistent with changes in carbon, and which can be used to obtain reasonable basin-integrated carbon uptake. With the addition of prior information about the distribution of boundary carbon fluxes, OTM shows considerable skill in recovering carbon fluxes that are closer to the model truth than the

345 prior, while also diagnosing inter-basin carbon transports consistent with the model. We will now discuss some limitations of the method, and the caveats and considerations relevant to its future application to observations.

A fundamental limitation of OTM stems from its use of a water mass coordinate system, from which it also derives its utility, but which necessitates some loss of information compared with, for example, the state estimation product we have used for its validation. Through the BSP binning process, we average tracer concentrations and their boundary fluxes over water masses,

350 and the method therefore does not resolve either tracer or flux gradients within a water mass. The effect of the latter is illustrated on Fig. 5, where we compare the unaltered ECCO-Darwin boundary carbon fluxes with the result of binning the fluxes into water mass space and then remapping them back into geographical coordinates using a mask (Eqs. 15, 17, and 19). Fig. 5b is the closest we can hope to get to the true model fluxes with this number of water masses (with the caveat noted in section 2.4 that we have remapped surface fluxes into three-dimensional water masses). In this validation, we divided each of 9 basins

355 into 64 water masses, chosen as a compromise between spatial resolution and required computing resources. In water mass coordinates, OTM is extremely computationally cheap by comparison with data-assimilation or Green's function approaches, obtaining solutions to the optimisation problem within a few seconds. However, the remapping back into geographical coordinates to aid interpretation of the results is more intensive, requiring the storage of large files containing the mask $\Omega(\mathbf{x}, t)$, and this places limits on the number of water masses that it is feasible to define.

360 In general, mass transports are unconstrained in OTM, beyond the mass conservation constraints in Eqs. 5 and 6; instead it is the conservation of tracers that provides the main constraints on the solutions. This constraint means that solutions may be obtained that are consistent with changes in temperature, salinity and carbon, but that are physically unrealistic in other ways. For example, if OTM needs to cool down a particular region through a flux of cold water, the method can achieve that either by fluxing a small amount of very cold water or a larger amount of moderately cold water into that region. Or similarly, to increase

365 the carbon concentration somewhere by some amount, this addition might be achieved either through a small flux of extremely carbon-rich water or a larger flux of less carbon-rich water. A possible impact of the lack of mass transport constraint was seen in the large counter-clockwise circulation of carbon on Fig. 8. In a future application, it may prove necessary to impose additional constraints on inter-basin mass transports; for example in the case of the South Pacific/Indian Ocean, it could be beneficial to further split the Southern Ocean in a manner that allows the imposition of an Antarctic Circumpolar Current.

370 Another avenue would be to impose some quasi-vertical structure on the inter-basin mass transports, which could be done in either temperature or salinity coordinates, or both.

We have placed subjective constraints on the connectivity between our 9 basins, such that all water masses in neighbouring basins are able to mix with one another, and that water masses from basins that are not neighbours cannot mix. This constraint might be too permissive in some places, for example allowing water masses from the Equatorial North Pacific to mix with those

375 in the Subtropical North Atlantic, or too strict in others, for example forbidding water masses from the Equatorial Atlantic that might be carried northwards in the western boundary current from mixing with those in the Polar North Atlantic. The fidelity of such constraints is also dependent on the timescale under consideration, which in our case was a decade between the 'early' and 'late' averaging periods, but could be shorter or longer.

Two further assumptions that have been subjectively imposed concern the boundary forcings. The first is that we have used

380 exact heat and freshwater forcings from ECCO-Darwin, thereby implicitly assuming these are known. Zika and Sohail (2023) already explored OTM's ability to recover boundary forcings of heat and freshwater from biased priors, and our focus was on the uptake, transport/mixing, and storage of carbon. However, when applying this technique to observations, there will be uncertainties on both the boundary forcings and the interior changes for all three tracers, and these errors will need to be considered. The second assumption relates to the order of action of boundary fluxes versus interior transports and mixing. In a

385 forward model such as ECCO-Darwin, time steps are discrete but comparatively short, such that boundary fluxes and interior transports and mixing occur effectively simultaneously, as they do in the real ocean. In the OTM framework, we have to make a choice about whether to apply the boundary forcing first and then calculate the transports and mixing required for the tracers to reach their 'late' distributions, or vice versa, or some combination of the two. In this study we have experimented with the first two possibilities for carbon, with our case 2-5 setups adopting the former (fluxes then mixing) and case 1 the latter (mixing

390 then fluxes), and found the former produced the best results.

4.2 Future application

There is one more component necessary for the future application of OTM to observations for the purposes of studying ocean carbon that we have yet to discuss: the inventory change. Temperature and salinity in the ocean is comparatively well observed, and their time evolution in the ocean interior has been mapped based on a combination of shipboard and Argo float observations

395 in the Met Office EN4 objective analysis (Good et al., 2013). By contrast, the ocean's interior carbon concentrations are considerably more sparsely sampled, with re-occupations of oceanographic sections collecting carbonate system variables usually taking place around once per decade (Gruber et al., 2023). Recently, products based on the first efforts to reconstruct the time-history of ocean interior carbon have emerged. These include a neural network technique similar to that employed by Landschützer et al. (2013) to map surface pCO_2, this time applied to DIC from the GLODAP database (Olsen et al.,

400 2019), to produce the 'MOBO-DIC' climatology (Keppler et al., 2020) and its time-varying successor (Keppler et al., 2023). Another approach, also using machine learning, by Zemskova et al. (2022) extrapolated from satellite data by combining it with numerical model output. Unfortunately, these two estimates are limited, respectively, to the top 1500 m of the ocean, and to the Southern Ocean only. A third technique developed by Turner et al. (2023) has been demonstrated as being able to reconstruct ocean interior carbon by ensemble optimal interpolation using only relationships between carbon, temperature,

405 salinity, and atmospheric CO_2 from models, but as yet no product applying this method to observations is available. The method does, nonetheless, demonstrate the plausibility of accurately reconstructing interior carbon from relationships to the better observed temperature and salinity fields, consistent with our findings from our 'case 1' experiment. We are working on producing our own global, full-depth, time-evolving estimates of DIC and C^* in the ocean, using machine learning with satellite and GLODAP data, which we hope by combining with OTM will enable us to produce the first global estimate of the

410 uptake, transport and storage of carbon directly from observations.

4.3 Conclusion

We have presented the application of a novel Optimal Transformation Method (OTM) to diagnosing the uptake, transport, and storage of carbon in the global ocean. The method utilises a balance between boundary forcings and interior transports and mixing in water mass space for conservative tracers, and we have validated it using outputs from the ECCO-Darwin

415 biogeochemical state estimate. When given prior estimates of the boundary forcing for carbon with biases based on reasonable observational uncertainties, OTM was able to recover the true carbon forcing and also to diagnose interior transports and mixing of heat, freshwater and carbon consistent with the model truth. When applied to observational reconstructions of changes in
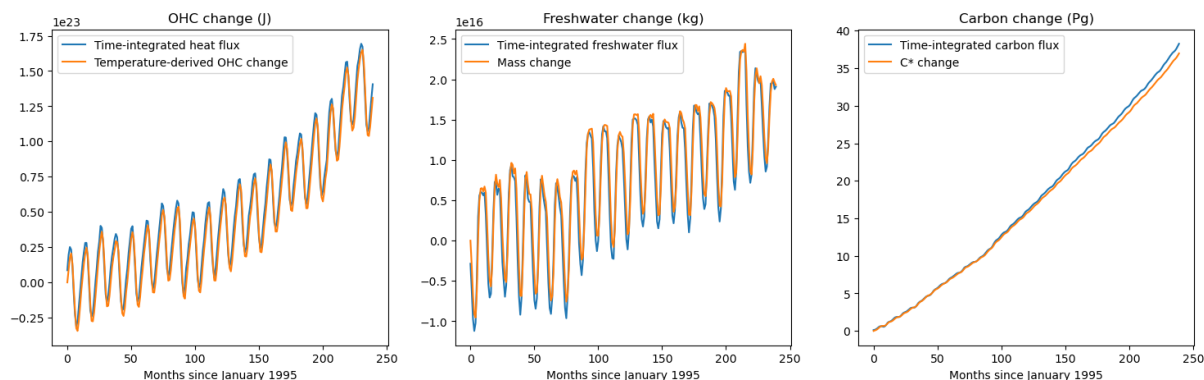
Figure A1. Budgets of ocean heat content (OHC; left), freshwater (middle) and carbon (right) from the result of BSP-binning ECCO-Darwin outputs for input to OTM. In blue are the sum of the boundary forcings, and in red the interior changes inferred from changes in T, S, and C^*.
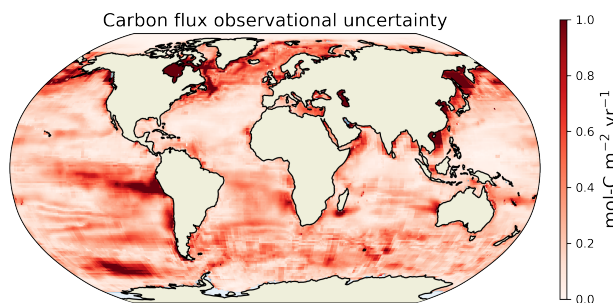
Figure A2. Observational uncertainties added to the carbon flux priors as described in section 2.3.

ocean carbon, OTM has the potential to reconcile changes in the interior anthropogenic carbon inventory with air-sea CO_2 fluxes through the action of physical transports and mixing.

420 *Code and data availability.* The ECCO-Darwin model data used for validation of the Optimal Transformation Method are available for download from https://data.nas.nasa.gov/ecco/index.html. The code used for producing and plotting the results presented is available on Zenodo with doi 10.5281/zenodo.10782587.

Table A1. Carbon budget for the case 2 OTM solution as plotted on Fig. 9. Values are in $\mathrm{Pg\,C\,yr^{-1}}$.

	Transport	Flux	Inventory Change
Polar N. Atlantic	-0.29	0.52	0.24
Subtropical N. Atlantic	0.05	0.00	0.05
Eq. Atlantic	0.11	-0.09	0.02
S. Atlantic	0.13	0.00	0.13
Indian	0.14	0.09	0.23
S. Pacific	0.03	-0.02	0.01
Eq. Pacific	0.70	-0.55	0.15
N. Pacific	-0.51	0.76	0.25
Southern Ocean	-0.36	1.14	0.79
TOTAL	0.00	1.88	1.88

Appendix A

A1

425   *Author contributions.* The Optimal Transformation Method was conceived by JDZ and developed by JDZ and TS. NM implemented its extension to carbon and carried out the validation in this study, with input from JDZ, TS, AJW, RW and OA. NM prepared the manuscript, adapting code created by TS to produce some of the figures. All authors contributed to the final text.

Competing interests. The authors declare no competing interests.

Acknowledgements. This work was supported by the National Environmental Research Council Grant NE/W001543/1. Andrew Watson is
430   additionally supported by Royal Society research professorship grants RP/EA/180008 and RP140106. For the purpose of open access, the author has applied a 'Creative Commons Attribution (CC BY) licence to any Author Accepted Manuscript version arising.
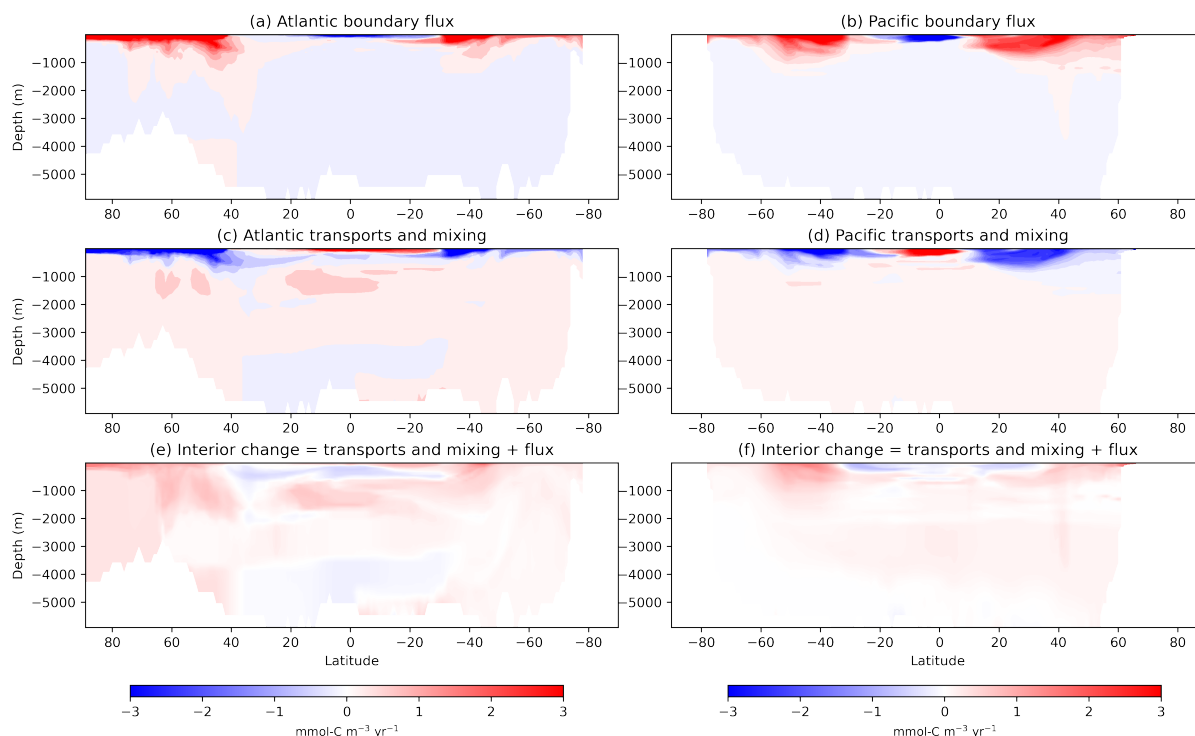
Figure A3. Full-depth zonally-averaged interior carbon concentration changes from the case 2 OTM solution in the Atlantic (left column) and the Pacific (right column). Top row shows the impact of carbon fluxes (either air-sea or sediment fluxes) in or out of the ocean; middle row shows the impact of transports and mixing on the carbon concentrations; and bottom row shows the interior changes, which is the sum of the first two rows. Positive values are increases in carbon concentrations between our early (1995-2005) and late (2005-2015) averaging periods due to each component, and negative values are decreases over that time.

References

Arora, V. K., Katavouta, A., Williams, R. G., Jones, C. D., Brovkin, V., Friedlingstein, P., Schwinger, J., Bopp, L., Boucher, O., Cadule, P., Chamberlain, M. A., Christian, J. R., Delire, C., Fisher, R. A., Hajima, T., Ilyina, T., Joetzjer, E., Kawamiya, M., Koven, C. D., Krasting, J. P., Law, R. M., Lawrence, D. M., Lenton, A., Lindsay, K., Pongratz, J., Raddatz, T., Séférian, R., Tachiiri, K., Tjiputra, J. F., Wiltshire, A., Wu, T., and Ziehn, T.: Carbon–concentration and carbon–climate feedbacks in CMIP6 models and their comparison to CMIP5 models, Biogeosciences, 17, 4173–4222, https://doi.org/10.5194/bg-17-4173-2020, 2020.

Bopp, L., Lévy, M., Resplandy, L., and Sallée, J. B.: Pathways of anthropogenic carbon subduction in the global ocean, Geophysical Research Letters, 42, 6416–6423, https://doi.org/10.1002/2015GL065073, 2015.

Caínzos, V., Hernández-Guerra, A., McCarthy, G. D., McDonagh, E. L., Cubas Armas, M., and Pérez-Hernández, M. D.: Thirty Years of GOSHIP and WOCE Data: Atlantic Overturning of Mass, Heat, and Freshwater Transport, Geophysical Research Letters, 49, 1–12, https://doi.org/10.1029/2021GL096527, 2022a.

Caínzos, V., Velo, A., Pérez, F. F., and Hernández-Guerra, A.: Anthropogenic Carbon Transport Variability in the Atlantic Ocean Over Three Decades, Global Biogeochemical Cycles, 36, https://doi.org/10.1029/2022GB007475, 2022b.

445 Carroll, D., Menemenlis, D., Adkins, J. F., Bowman, K. W., Brix, H., Dutkiewicz, S., Fenty, I., Gierach, M. M., Hill, C., Jahn, O., Landschützer, P., Lauderdale, J. M., Liu, J., Manizza, M., Naviaux, J. D., Rödenbeck, C., Schimel, D. S., Van der Stocken, T., and Zhang, H.: The ECCO-Darwin Data-Assimilative Global Ocean Biogeochemistry Model: Estimates of Seasonal to Multidecadal Surface Ocean pCO2 and Air-Sea CO2 Flux, Journal of Advances in Modeling Earth Systems, 12, 1–28, https://doi.org/10.1029/2019MS001888, 2020.

Carroll, D., Menemenlis, D., Dutkiewicz, S., Lauderdale, J. M., Adkins, J. F., Bowman, K. W., Brix, H., Fenty, I., Gierach, M. M.,
450 Hill, C., Jahn, O., Landschützer, P., Manizza, M., Mazloff, M. R., Miller, C. E., Schimel, D. S., Verdy, A., Whitt, D. B., and Zhang, H.: Attribution of Space-Time Variability in Global-Ocean Dissolved Inorganic Carbon, Global Biogeochemical Cycles, 36, 1–12, https://doi.org/10.1029/2021GB007162, 2022.

DeVries, T., Holzer, M., and Primeau, F.: Recent increase in oceanic carbon uptake driven by weaker upper-ocean overturning, Nature, 542, 215–218, https://doi.org/10.1038/nature21068, 2017.

455 Doney, S. C., Fabry, V. J., Feely, R. A., and Kleypas, J. A.: Ocean Acidification: The Other CO2 Problem, Annual Review of Marine Science, 1, 169–192, https://doi.org/10.1146/annurev.marine.010908.163834, 2009.

Dutkiewicz, S., Hickman, A. E., Jahn, O., Gregg, W. W., Mouw, C. B., and Follows, M. J.: Capturing optically important constituents and properties in a marine biogeochemical and ecosystem model, Biogeosciences, 12, 4447–4481, https://doi.org/10.5194/bg-12-4447-2015, 2015.

460 Evans, G., McDonagh, E., King, B., Bryden, H., Bakker, D., Brown, P., Schuster, U., Speer, K., and van Heuven, S.: South Atlantic interbasin exchanges of mass, heat, salt and anthropogenic carbon, Progress in Oceanography, 151, 62–82, https://doi.org/10.1016/j.pocean.2016.11.005, 2017.

Fay, A. R. and McKinley, G. A.: Observed Regional Fluxes to Constrain Modeled Estimates of the Ocean Carbon Sink, Geophysical Research Letters, 48, 1–11, https://doi.org/10.1029/2021GL095325, 2021.

465 Fay, A. R., Gregor, L., Landschützer, P., McKinley, G. A., Gruber, N., Gehlen, M., Iida, Y., Laruelle, G. G., Rödenbeck, C., Roobaert, A., and Zeng, J.: SeaFlux: harmonization of air-sea CO2 fluxes from surface pCO2 data products using a standardized approach, Earth System Science Data, 13, 4693–4710, https://doi.org/10.5194/essd-13-4693-2021, 2021.

Forget, G., Campin, J.-M., Heimbach, P., Hill, C. N., Ponte, R. M., and Wunsch, C.: ECCO version 4: an integrated framework for non-linear inverse modeling and global ocean state estimation, Geoscientific Model Development, 8, 3071–3104, https://doi.org/10.5194/gmd-8-
470 3071-2015, 2015.

Friedlingstein, P., O'Sullivan, M., Jones, M. W., Andrew, R. M., Gregor, L., Hauck, J., Le Quéré, C., Luijkx, I. T., Olsen, A., Peters, G. P., Peters, W., Pongratz, J., Schwingshackl, C., Sitch, S., Canadell, J. G., Ciais, P., Jackson, R. B., Alin, S. R., Alkama, R., Arneth, A., Arora, V. K., Bates, N. R., Becker, M., Bellouin, N., Bittig, H. C., Bopp, L., Chevallier, F., Chini, L. P., Cronin, M., Evans, W., Falk, S., Feely, R. A., Gasser, T., Gehlen, M., Gkritzalis, T., Gloege, L., Grassi, G., Gruber, N., Gürses, Ö., Harris, I., Hefner, M., Houghton, R. A., Hurtt,
475 G. C., Iida, Y., Ilyina, T., Jain, A. K., Jersild, A., Kadono, K., Kato, E., Kennedy, D., Klein Goldewijk, K., Knauer, J., Korsbakken, J. I., Landschützer, P., Lefèvre, N., Lindsay, K., Liu, J., Liu, Z., Marland, G., Mayot, N., McGrath, M. J., Metzl, N., Monacci, N. M., Munro, D. R., Nakaoka, S.-I., Niwa, Y., O'Brien, K., Ono, T., Palmer, P. I., Pan, N., Pierrot, D., Pocock, K., Poulter, B., Resplandy, L., Robertson, E., Rödenbeck, C., Rodriguez, C., Rosan, T. M., Schwinger, J., Séférian, R., Shutler, J. D., Skjelvan, I., Steinhoff, T., Sun, Q., Sutton, A. J., Sweeney, C., Takao, S., Tanhua, T., Tans, P. P., Tian, X., Tian, H., Tilbrook, B., Tsujino, H., Tubiello, F., van der Werf, G. R., Walker,

480   A. P., Wanninkhof, R., Whitehead, C., Willstrand Wranne, A., Wright, R., Yuan, W., Yue, C., Yue, X., Zaehle, S., Zeng, J., and Zheng, B.:
Global Carbon Budget 2022, Earth System Science Data, 14, 4811–4900, https://doi.org/10.5194/essd-14-4811-2022, 2022.

Good, S. A., Martin, M. J., and Rayner, N. A.: EN4: Quality controlled ocean temperature and salinity profiles and monthly objective analyses
with uncertainty estimates, Journal of Geophysical Research: Oceans, 118, 6704–6716, https://doi.org/10.1002/2013JC009067, 2013.

Grist, J. P., Josey, S. A., Zika, J. D., Evans, D. G., and Skliris, N.: Assessing recent air-sea freshwater flux changes using a surface temperature-
485   salinity space framework, Journal of Geophysical Research: Oceans, 121, 8787–8806, https://doi.org/10.1002/2016JC012091, 2016.

Groeskamp, S., Zika, J. D., Sloyan, B. M., McDougall, T. J., and McIntosh, P. C.: A Thermohaline Inverse Method for Estimating Diather-
mohaline Circulation and Mixing, Journal of Physical Oceanography, 44, 2681–2697, https://doi.org/10.1175/JPO-D-14-0039.1, 2014.

Groeskamp, S., Griffies, S. M., Iudicone, D., Marsh, R., Nurser, A. G., and Zika, J. D.: The Water Mass Transformation Framework for Ocean
Physics and Biogeochemistry, Annual Review of Marine Science, 11, 271–305, https://doi.org/10.1146/annurev-marine-010318-095421,
490   2019.

Gruber, N., Sarmiento, J. L., and Stocker, T. F.: An improved method for detecting anthropogenic CO2 in the oceans, Global Biogeochemical
Cycles, 10, 809–837, https://doi.org/10.1029/96GB01608, 1996.

Gruber, N., Clement, D., Carter, B. R., Feely, R. A., van Heuven, S., Hoppema, M., Ishii, M., Key, R. M., Kozyr, A., Lauvset, S. K., Monaco,
C. L., Mathis, J. T., Murata, A., Olsen, A., Perez, F. F., Sabine, C. L., Tanhua, T., and Wanninkhof, R.: The oceanic sink for anthropogenic
495   CO2 from 1994 to 2007, Science, 363, 1193–1199, https://doi.org/10.1126/science.aau5153, 2019.

Gruber, N., Bakker, D. C., DeVries, T., Gregor, L., Hauck, J., Landschützer, P., McKinley, G. A., and Müller, J. D.: Trends and variability in
the ocean carbon sink, Nature Reviews Earth and Environment, 4, 119–134, https://doi.org/10.1038/s43017-022-00381-x, 2023.

Haine, T. W. N. and Hall, T. M.: A Generalized Transport Theory: Water-Mass Composition and Age, Journal of Physical Oceanography,
32, 1932–1946, https://doi.org/10.1175/1520-0485(2002)032<1932:AGTTWM>2.0.CO;2, 2002.

500   Halloran, P. R., Booth, B. B. B., Jones, C. D., Lambert, F. H., McNeall, D. J., Totterdell, I. J., and Völker, C.: The mechanisms
of North Atlantic CO₂ uptake in a large Earth System Model ensemble, Biogeosciences, 12, 4497–4508,
https://doi.org/10.5194/bg-12-4497-2015, 2015.

Hauck, J., Zeising, M., Le Quéré, C., Gruber, N., Bakker, D. C. E., Bopp, L., Chau, T. T. T., Gürses, Ö., Ilyina, T., Landschützer, P., Lenton,
A., Resplandy, L., Rödenbeck, C., Schwinger, J., and Séférian, R.: Consistency and Challenges in the Ocean Carbon Sink Estimate for the
505   Global Carbon Budget, Frontiers in Marine Science, 7, 1–22, https://doi.org/10.3389/fmars.2020.571720, 2020.

Hieronymus, M., Nilsson, J., and Nycander, J.: Water Mass Transformation in Salinity–Temperature Space, Journal of Physical Oceanogra-
phy, 44, 2547–2568, https://doi.org/10.1175/JPO-D-13-0257.1, 2014.

Keppler, L., Landschützer, P., Gruber, N., Lauvset, S. K., and Stemmler, I.: Seasonal Carbon Dynamics in the Near-Global Ocean, Global
Biogeochemical Cycles, 34, https://doi.org/10.1029/2020GB006571, 2020.

510   Keppler, L., Landschützer, P., Lauvset, S. K., and Gruber, N.: Recent Trends and Variability in the Oceanic Storage of Dissolved Inorganic
Carbon, Global Biogeochemical Cycles, 37, https://doi.org/10.1029/2022GB007677, 2023.

Khatiwala, S., Primeau, F., and Hall, T.: Reconstruction of the history of anthropogenic CO2 concentrations in the ocean, Nature, 462,
346–349, https://doi.org/10.1038/nature08526, 2009.

Landschützer, P., Gruber, N., Bakker, D. C. E., Schuster, U., Nakaoka, S., Payne, M. R., Sasse, T. P., and Zeng, J.: A neural
515   network-based estimate of the seasonal to inter-annual variability of the Atlantic Ocean carbon sink, Biogeosciences, 10, 7793–7815,
https://doi.org/10.5194/bg-10-7793-2013, 2013.

Mackay, N., Wilson, C., Zika, J., and Holliday, N. P.: A Regional Thermohaline Inverse Method for Estimating Circulation and Mixing in the Arctic and Subpolar North Atlantic, Journal of Atmospheric and Oceanic Technology, 35, 2383–2403, https://doi.org/10.1175/JTECH-D-17-0198.1, 2018.

520 Nurser, A. J. G., Marsh, R., and Williams, R. G.: Diagnosing Water Mass Formation from Air–Sea Fluxes and Surface Mixing, Journal of Physical Oceanography, 29, 1468–1487, https://doi.org/10.1175/1520-0485(1999)029<1468:DWMFFA>2.0.CO;2, 1999.

Olsen, A., Lange, N., Key, R. M., Tanhua, T., Álvarez, M., Becker, S., Bittig, H. C., Carter, B. R., Cotrim da Cunha, L., Feely, R. A., van Heuven, S., Hoppema, M., Ishii, M., Jeansson, E., Jones, S. D., Jutterström, S., Karlsen, M. K., Kozyr, A., Lauvset, S. K., Lo Monaco, C., Murata, A., Pérez, F. F., Pfeil, B., Schirnick, C., Steinfeldt, R., Suzuki, T., Telszewski, M., Tilbrook, B., Velo, A., and Wanninkhof, R.:
525 GLODAPv2.2019 – an update of GLODAPv2, Earth System Science Data, 11, 1437–1461, https://doi.org/10.5194/essd-11-1437-2019, 2019.

Pemberton, P., Nilsson, J., Hieronymus, M., and Markus Meier, H. E.: Arctic ocean water mass transformation in S-T coordinates, Journal of Physical Oceanography, 45, 1025–1050, https://doi.org/10.1175/JPO-D-14-0197.1, 2015.

Rödenbeck, C., Bakker, D. C. E., Gruber, N., Iida, Y., Jacobson, A. R., Jones, S., Landschützer, P., Metzl, N., Nakaoka, S., Olsen, A., Park,
530 G.-H., Peylin, P., Rodgers, K. B., Sasse, T. P., Schuster, U., Shutler, J. D., Valsala, V., Wanninkhof, R., and Zeng, J.: Data-based estimates of the ocean carbon sink variability – first results of the Surface Ocean p CO 2 Mapping intercomparison (SOCOM), Biogeosciences, 12, 7251–7278, https://doi.org/10.5194/bg-12-7251-2015, 2015.

Sohail, T., Irving, D. B., Zika, J. D., Holmes, R. M., and Church, J. A.: Fifty Year Trends in Global Ocean Heat Content Traced to Surface Heat Fluxes in the Sub-Polar Ocean, Geophysical Research Letters, 48, https://doi.org/10.1029/2020GL091439, 2021.

535 Sohail, T., Holmes, R. M., and Zika, J.: Watermass Co-Ordinates Isolate the Historical Ocean Warming Signal, Journal of Climate, pp. 1–40, https://doi.org/10.1175/jcli-d-22-0363.1, 2023.

Speer, K. G.: Conversion among North Atlantic surface water types, Tellus A, 45, 72–79, https://doi.org/10.1034/j.1600-0870.1993.00006.x, 1993.

Turner, K. E., Smith, D. M., Katavouta, A., and Williams, R. G.: Reconstructing ocean carbon storage with CMIP6 Earth system models and
540 synthetic Argo observations, Biogeosciences, 20, 1671–1690, https://doi.org/10.5194/bg-20-1671-2023, 2023.

Walin, G.: On the relation between sea-surface heat flow and thermal circulation in the ocean, Tellus, 34, 187–195, https://doi.org/10.3402/tellusa.v34i2.10801, 1982.

Watson, A. J., Schuster, U., Shutler, J. D., Holding, T., Ashton, I. G., Landschützer, P., Woolf, D. K., and Goddijn-Murphy, L.: Revised estimates of ocean-atmosphere CO2 flux are consistent with ocean carbon inventory, Nature Communications, 11, 1–6,
545 https://doi.org/10.1038/s41467-020-18203-3, 2020.

Zemskova, V. E., He, T. L., Wan, Z., and Grisouard, N.: A deep-learning estimate of the decadal trends in the Southern Ocean carbon storage, Nature Communications, 13, https://doi.org/10.1038/s41467-022-31560-5, 2022.

Zika, J. D. and Sohail, T.: An optimal transformation method for inferring ocean tracer sources and sinks, EGUsphere [preprint], https://doi.org/https://doi.org/10.5194/egusphere-2023-1220, 2023.

550 Zika, J. D., England, M. H., and Sijp, W. P.: The Ocean Circulation in Thermohaline Coordinates, Journal of Physical Oceanography, 42, 708–724, https://doi.org/10.1175/JPO-D-11-0139.1, 2012.

Zika, J. D., Gregory, J. M., McDonagh, E. L., Marzocchi, A., and Clément, L.: Recent water mass changes reveal mechanisms of ocean warming, Journal of Climate, 34, 3461–3479, https://doi.org/10.1175/JCLI-D-20-0355.1, 2021.